

# Nuclear Matter Equation of State in the Brueckner-Hartree-Fock Approach and Standard Skyrme Energy-Density Functionals

Isaac Vidaña <sup>1,‡</sup>, Jérôme Margueron <sup>2,3,\*</sup>, and Hans-Josef Schulze <sup>1,‡</sup>

<sup>1</sup> Istituto Nazionale di Fisica Nucleare, Sezione di Catania, Dipartimento di Fisica e Astronomia “Ettore Majorana”, Università di Catania, Via Santa Sofia 64, I-95123 Catania, Italy

<sup>2</sup> Institut de Physique Nucléaire, Université Lyon 1 and CNRS/IN2P3, 4 rue Enrico Fermi, 69622 Villeurbanne, France

<sup>3</sup> International Research Laboratory on Nuclear Physics and Astrophysics, Michigan State University and CNRS, East Lansing, MI 48824, USA

\* Correspondence: jerome.margueron@cnrs.fr

‡ These authors contributed equally to this work.

**Abstract:** The equation of state of asymmetric nuclear matter as well as the neutron and proton effective masses and their partial-wave and spin-isospin decomposition are analyzed within the Brueckner–Hartree–Fock approach. Theoretical uncertainties for all these quantities are estimated by using several phase-shift-equivalent nucleon-nucleon forces together with two types of three-nucleon forces, phenomenological and microscopic. It is shown that the choice of the three-nucleon force plays an important role above saturation density, leading to different density dependencies of the energy per particle. These results are compared to the standard form of the Skyrme energy-density functional and we find that it is not possible to reproduce the BHF predictions in the ( $S, T$ ) channels in symmetric and neutron matter above saturation density, already at the level of the two-body interaction, and even more including the three-body interaction.

**Keywords:** nuclear matter; equation of state; effective mass

## 1. Introduction

A new era of multi-messenger astronomy has begun with the first detection of gravitational wave signals, also known as GW170817 or AT2017gfo for the electromagnetic emission originating from the kilonova formed by the binary neutron star merger [1,2]. This new astronomy emphasizes the crucial role of neutron stars (NSs), which are prototypes for the most extreme phases of matter where the strong, the weak, the gravitational and the electromagnetic interactions can be studied in regimes that cannot be explored on Earth. In this paper, we are analyzing the properties of the dense-matter equation of state (EOS) from microscopic calculations with a focus on the strong three-body interaction and we discuss the link with empirical energy density functionals (EDFs).

In recent years, the determination of nuclear EDFs incorporates more and more information deduced from microscopic calculations of nuclear matter. Usually, one specific or a very limited number of microscopic calculations are considered in the fitting protocols. However, the impact of the choices of the bare nuclear interaction, the regularization scheme, the experimental error in the phase shift data, and of the many-body framework is important, and has been cautiously addressed in the chiral effective field theory ( $\chi$ -EFT) [3] in order to theoretically predict the nuclear EOS including error estimates. There is however an upper limit on density (presently estimated to be  $(1-2)n_{\text{sat}}$  with  $n_{\text{sat}} \approx 0.155 \pm 0.005 \text{ fm}^{-3}$  [4]), where the chiral EFT breaks down and also the error estimates become meaningless [5–7].

At increasing density – and already around  $n_{\text{sat}}$  – also the role of nuclear three-body forces (3BF) in nuclear matter cannot be ignored. For traditional meson-exchange potential models, the compatible 3BF correction at saturation density is of limited magnitude, a few

**Citation:** Vidaña, I.; Margueron, J.; Schulze, H.-J. Nuclear Matter Equation of State. *Universe* **2024**, *1*, 0. <https://doi.org/>

Received:

Accepted:

Published:

**Copyright:** © 2024 by the authors. Submitted to *Universe* for possible open access publication under the terms and conditions of the Creative Commons Attribution (CC BY) license (<https://creativecommons.org/licenses/by/4.0/>).

MeV, which represents (15–20)% of the total energy, in order to reproduce the saturation of nuclear matter. With the advent of regularized soft-core nuclear interactions, such as  $V_{\text{low-k}}$  [8] as well as chiral effective field theory ( $\chi$ -EFT) [3], a new paradigm has emerged. In short, any modification of the two-body interaction, by applying a unitary transformation, generates many-body interactions. The 3BF cannot be viewed as independent of the two-body force (2BF), but instead, it contains a part of the repulsive hard-core interaction. Regularized soft-core interactions need stronger many-body interactions to saturate, compared to the hard-core ones.

Building bridges between EDFs for the in-medium nuclear interaction and microscopic approaches of the nuclear many-body problem is, therefore, fundamental for a consistent understanding of nuclei, neutron stars, core-collapse supernovae, and kilonovae. Microscopic approaches, on one hand, have the advantage of being based on realistic 2BFs that reproduce with high precision the scattering phase shifts and the deuteron properties, and include the isospin asymmetry dependence in a natural way. However, the direct implementation of microscopic approaches in finite nuclei is not an easy task. A realistic 2BF cannot be used directly in nuclei. Its hard-core repulsion requires a resummation as in uniform matter and 3BFs are required to describe both the energy and charge radii of finite nuclei. EDF models, on the other hand, are usually based on effective density-dependent interactions with parameters frequently fitted to reproduce global properties of nuclei and properties of symmetric and neutron matter [9–11]. These effective interactions capture the essence of the in-medium nuclear interaction as well as the effect of the complex correlations. Their predictions at high densities and isospin asymmetries, however, should be taken with care and discussed in view of the considered constraints. Combining phenomenological models with microscopic approaches would, therefore, help in setting up a nuclear model based on realistic 2BFs and 3BFs that can simultaneously describe the properties of nuclei and those of infinite nuclear matter in a large range of densities and isospin asymmetries.

Two major sources of uncertainty arise, however, when trying to build links between EDFs and microscopic approaches. The first is that there is a fairly large number of realistic 2BFs that reproduce the scattering data and the deuteron properties with equivalent high accuracy. Predictions employing these interactions shall then be compared to estimate the uncertainty due to the nuclear interaction (leading to an estimate of systematic uncertainties). The second source of uncertainties is due to the different methods employed to solve the nuclear many-body problem (which also contributes to systematical uncertainties). A critical comparison of various microscopic approaches using the same 2BF has been performed in Ref. [12]. The aim of this work is to find the sources of discrepancies, and ultimately to determine a “systematic uncertainty” associated with the different microscopic approaches of the nuclear-matter EOS. The approaches considered were the Brueckner–Hartree–Fock (BHF) [13], the Brueckner–Bethe–Goldstone (BBG) expansion up to third order [14], the self-consistent Green’s function (SCGF) [15], the auxiliary field diffusion Monte Carlo (AFDMC) [16], the Green’s function Monte Carlo (GFMC) [17], and the Fermi hypernetted chain (FHNC) [18]. The properties of pure neutron matter (NM) and symmetric nuclear matter (SM) were computed with simplified versions [19] of the widely used Argonne Av18 potential [20], and a careful comparison of the results obtained with the different approaches was performed. The results of this work confirmed that the tensor and spin-orbit components of the 2BF and their in-medium treatment are responsible for most of the observed discrepancies among these approaches [12]. A very similar study has been performed recently in Refs. [21,22].

The EDF models adjusted to microscopic approaches shall incorporate these sources of uncertainties in the microscopic predictions for dense matter. Several authors have already determined EDF models from microscopic approaches (see, e.g., Refs. [10,23–28]). The authors of Ref. [23], for instance, constructed a Skyrme-type EDF based on BHF results for infinite matter and applied it to a set of isospin-symmetric and asymmetric nuclei through the mass table. Their results provided a microscopic basis for a link between nuclear surface behavior and the NM EOS, as previously observed with phenomenological

effective forces. The same authors have also developed the so-called Barcelona-Catania-Paris-Madrid (BCPM) EDF [24] obtained from BHF calculations of nuclear matter within an approximation inspired by the Kohn-Sham formulation of density functional theory [29]. The BCPM EDF is built with a bulk part obtained directly from BHF results for NM and SM via a local-density approximation, and is supplemented by a phenomenological surface part together with the Coulomb, spin-orbit, and pairing contributions. The functional, with four adjustable parameters, is able to describe the ground-state properties of finite nuclei with an accuracy comparable to that of Skyrme and Gogny forces.

Later on, the so-called LNS Skyrme force was built in Ref. [25] based also on BHF calculations of infinite nuclear matter with consistent 2BFs and 3BFs. It was further refined in Ref. [27] to reproduce experimental binding energies and charge radii of some selected nuclei. A similar fitting procedure was also used in Ref. [10], where various Skyrme forces were adjusted to the  $(S, T)$  decomposition of the results of two different BHF calculations [30,31]<sup>1</sup>. The comparison of the two microscopic calculations provided a kind of theoretical uncertainty based on the 2BFs and 3BFs employed, and suggests that the associated differences should be carefully analyzed. In Ref. [28] the tensor contribution to the  $(S, T)$  channels and different partial waves was analyzed. However, similarly to previous works, the uncertainty of the microscopic calculations was not included in the determination of the EDF. Finally let us mention the analysis of Quantum Monte Carlo (QMC) calculations of spin-polarized neutron matter, which have been compared to predictions of several Skyrme EDFs [32]. Such analysis allowed to probe the time-odd part of the Skyrme EDFs independently of the time-even one and was found to be very constraining. Also here an estimate of the uncertainty of the microscopic calculation would be very valuable, in particular as the density of the medium increases.

In the present paper, we aim to provide an estimation of the uncertainty of the nuclear EOS predicted by the BHF approach up to about  $0.4 \text{ fm}^{-3} \gtrsim 2n_{\text{sat}}$  based on several nuclear two- and three-body interactions. Special attention is paid to the impact of the latter ones for which we consider two different types: phenomenological and microscopical 3BF. We then determine the corresponding parameter ranges of Skyrme-type nuclear energy density functionals, and more importantly, we show that the BHF calculations in the different  $(S, T)$  channels in SM and NM cannot be reproduced by the Skyrme EDF above  $n_{\text{sat}}$ , already from the 2BF results.

The paper is organized as follows. In section 2 a brief review of the BHF approach is presented. The  $(S, T)$  and partial-wave decomposition of the BHF correlation energy per particle for SM and NM is analysed in section 3. In section 4 this decomposition is employed to constrain the parameters of Skyrme-type forces. A summary and the main conclusions are given in section 5.

## 2. BHF approach of nuclear matter

The BHF approach is the lowest-order realization of the BBG many-body theory of nuclear matter [33]. In this theory, the ground-state energy of nuclear matter is evaluated in terms of the so-called hole-line expansion, where the perturbative diagrams are grouped according to the number of independent hole-lines. The expansion is derived by means of the in-medium two-body scattering matrix  $G$ , which describes the effective interaction between two nucleons in the presence of a surrounding medium. The  $G$  matrix is obtained by solving the well-known Bethe-Goldstone equation

$$\langle i'j'|G|ij\rangle = \langle i'j'|V|ij\rangle + \frac{1}{\Omega} \sum_{ml} \langle i'j'|V|ml\rangle \frac{Q_{ml}}{\varepsilon_i + \varepsilon_j - \varepsilon_m - \varepsilon_l + i\eta} \langle ml|G|ij\rangle, \quad (1)$$

where the multi-indices  $i, j, m, l, i', j'$  indicate all the quantum numbers (momentum  $k$ , spin  $\sigma$  and isospin  $\tau$  projections) characterizing the two nucleons in the initial, intermediate,

<sup>1</sup> Note that in Fig.7 of Ref. [10] the BHF predictions for the  $(S, T)$  channels  $(0, 1)$  and  $(1, 1)$  in SM from catania2 [30] results have been exchanged.

and final states,  $V$  denotes the bare  $NN$  interaction,  $\Omega$  is the (large) volume enclosing the system,  $Q_{ml} = (1 - f_m)(1 - f_l)$  with  $f_i = \theta(k_F^{(\tau_i)} - |k_i|)$  is the Pauli operator taking into account the effect of the exclusion principle on the scattered holes, and  $k_F^{(\tau_i)} = (3\pi^2 n_{\tau_i})^{1/3}$  is the Fermi momentum for particle  $i$  with density  $n_{\tau_i}$  defined in the ground state. The single-particle (s.p.) energy of a nucleon with momentum  $k_i$  and isospin  $\tau_i$  is

$$\varepsilon_i \equiv \varepsilon_{\tau_i}(k_i) = \frac{k_i^2}{2m_{\tau_i}} + \text{Re}U_{\tau_i}(k_i), \quad (2)$$

being  $U_{\tau_i}(k_i)$  the mean field felt by the nucleon  $i$  due to its interaction with the other nucleons of the medium. In the BHF approximation it is calculated through the “on-shell”  $G$ -matrix,

$$U_{\tau_i}(k_i) = \frac{1}{\Omega} \sum_j f_j \langle ij | G | ij \rangle_a, \quad (3)$$

where the matrix elements are meant to be properly antisymmetrized. Note that Eqs. (1,2,3) should be solved self-consistently. The momentum dependence of the s.p. energy  $\varepsilon_{\tau_i}$  can be characterized in terms of the effective mass [34],

$$\frac{m_{\tau_i}^*(k_i)}{m} = \frac{k_i}{m} \left( \frac{d\varepsilon_{\tau_i}}{dk_i} \right)^{-1}. \quad (4)$$

We consider in the following isospin-asymmetric nuclear matter and for clarity we shall specify the isospin index  $\tau$ . However, since we will discuss only spin-symmetric matter, the spin up and down potentials are equal and we do not specify the spin index in the following. For simplicity we consider the same bare mass for neutrons and protons  $m_{\tau} = (m_n + m_p)/2 \equiv m$ .

In the BHF approach, the total energy per particle of nuclear matter is given by the sum of only two-hole-line diagrams that include the effect of two-body correlations through the  $G$  matrix,

$$E_{\text{tot}} = \frac{1}{n} \sum_i f_i \frac{k_i^2}{2m} + \frac{1}{2n\Omega} \sum_{ij} f_i f_j \text{Re} \langle ij | G | ij \rangle_a = \frac{1}{n} \sum_i f_i \frac{k_i^2}{2m} + E_{\text{cor}}, \quad (5)$$

where the first term on the right hand side is the energy of a free Fermi gas and the second one is the so-called BHF correlation energy,  $E_{\text{cor}}$ . We note here that the latter is usually referred to as BHF potential energy.

It has been shown in Ref. [14] for the  $V_{18}$ , and recently confirmed in Ref. [35] for several modern 2BFs, that the contribution to the total energy from three-hole-line diagrams (which account for the effect of three-body correlations) is minimized when the so-called continuous prescription [34] is adopted for the BHF s.p. energy (2). This is a strong indication of the convergence of the hole-line expansion around saturation density and above. We adopt this prescription in our calculations and limit the exploration to densities less than  $0.4 \text{ fm}^{-3}$ , where the hole-line expansion parameter  $\kappa = (c/d)^3$  (with  $c$  the interaction range and  $d$  the average distance between two nucleons) is still sufficiently small [35,36].

The present BHF calculations are carried out using a set of several phase-shift-equivalent  $NN$  potentials, namely, Av18 [37], NSC97a-f [38], a non-relativistic version of the Bonn B potential (Bonn) [39] and the charge-dependent Bonn potential (CD-Bonn) [40]. The predictions for the nuclear EOS based on these 2BFs are grouped together under the name 2BF. The group 2+3BFph assemble the predictions of the same 2BF interactions supplemented with a 3BF of Urbana type [41] consisting of the sum of the attractive two-pion-exchange Fujita–Miyazawa force with excitation of an intermediate  $\Delta$ -resonance [42] plus a phenomenological repulsive term. The group 2+3BFmic is a set of microscopic potentials [43] based on the Av18, Bonn B, or Nijmegen93 [44] potentials, which are also used to calculate consistently a three-body potential including the virtual excitation of  $\Delta(1232)$  and  $N^*(1440)$

**Table 1.** Partial-wave contributions to the different  $(S, T)$  channels using the spectroscopic notation  $2S+1L_J$ .

Name	$(S, T)$	L	Partial waves	Legend in Figs. 2 and 3
Singlet Odd SO	(0,0)	1	$^1P_1$	P
		3	$^1F_3$	F
		5	$^1H_5$	H
		7	$^1J_7$	J
Singlet Even SE	(0,1)	0	$^1S_0$	S
		2	$^1D_2$	D
		4	$^1G_4$	G
		6	$^1I_6$	I
Triplet Even TE	(1,0)	0	$^3S_1$	S
		2	$^3D_{1,2,3}$	D
		4	$^3G_{3,4,5}$	G
		6	$^3I_{5,6,7}$	I
Triplet Odd TO	(1,1)	1	$^3P_{0,1,2}$	P
		3	$^3F_{2,3,4}$	F
		5	$^3H_{4,5,6}$	H
		7	$^3J_{6,7,8}$	J

resonances and anti-nucleons. In both cases, for the use in the BHF approach, these 3BF have been reduced to an effective two-nucleon density-dependent force by averaging over the coordinates of the third nucleon [45]. The interested reader is referred to Refs. [43,46–48] for an extensive analysis of the use and effects of 3BF in nuclear matter.

### 3. Results of Brueckner–Hartree–Fock microscopic calculations

We discuss in this section the results of the BHF calculations of nuclear matter.

#### 3.1. Correlation energy per particle

In the BHF approach the correlation energy per particle  $E_{\text{cor}}$ , last term of Eq. (5), can be easily linked to the spin-isospin and the partial-wave decomposition of the  $G$ -matrix, providing an interesting insight into the impact of the different  $(S, T)$  channels and partial waves contributing to the nuclear EOS. With the aim of providing more stringent constraints for phenomenological EDFs, we analyze in this section these decompositions for both SM and NM. A particular application of these constraints to a Skyrme force is discussed in the next section.

##### 3.1.1. Spin-isospin decomposition of the correlation energy

The spin-isospin decomposition of the correlation energy per particle reads

$$E_{\text{cor}} = \sum_{S,T} E_{\text{cor}}^{(S,T)}, \quad (6)$$

where the contribution of each  $(S, T)$  channel,

$$E_{\text{cor}}^{(S,T)} = \frac{1}{2n\Omega} \sum_{ij} f_i f_j \text{Re} \langle ij | GP_S P_T | ij \rangle_a, \quad (7)$$

can be obtained by using the projectors on spin and isospin singlet and triplet states,  $P_S = \frac{1}{2}[1 + (S - \frac{1}{2})(1 + \sigma_1 \cdot \sigma_2)]$  and  $P_T = \frac{1}{2}[1 + (T - \frac{1}{2})(1 + \tau_1 \cdot \tau_2)]$ . The partial waves contributing to the different channels are listed in table 1.

The density dependence of the spin-isospin  $(S, T)$  decomposition of  $E_{\text{cor}}$  in SM and NM is shown in Fig. 1, where the bands correspond to the uncertainty associated with the different models used in our BHF calculation, as previously discussed. The dotted and

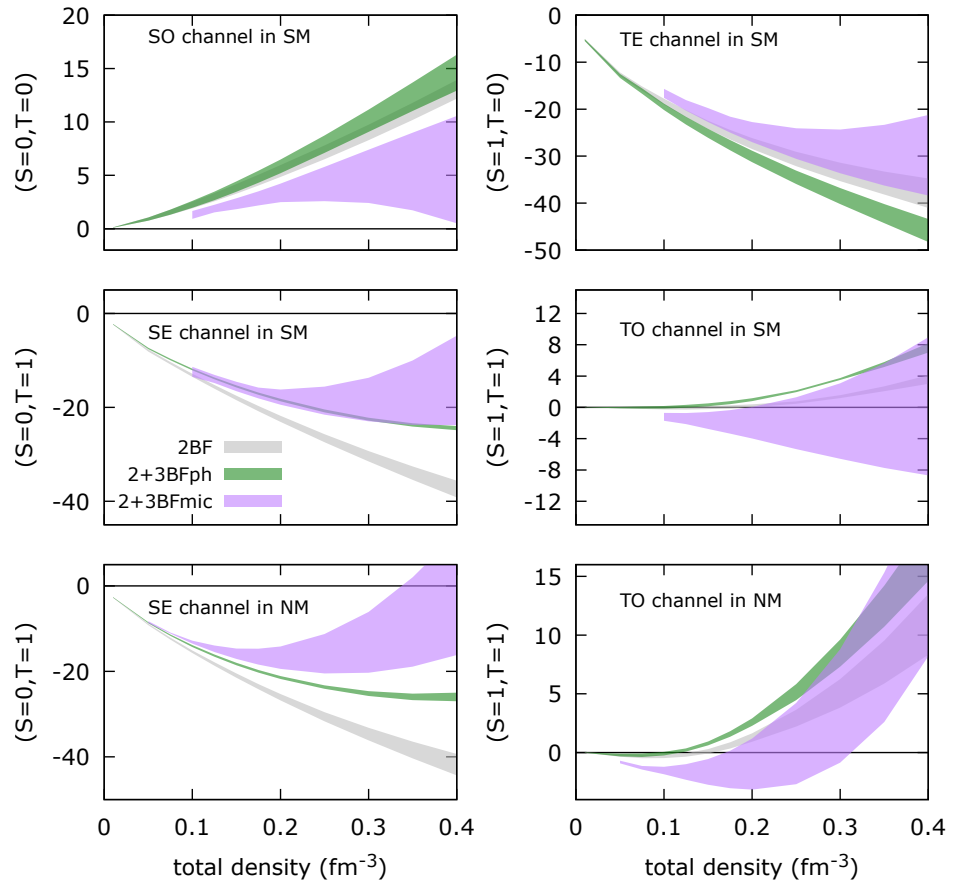


**Figure 1.** Spin-isospin ( $S, T$ ) channel decomposition of the correlation energy per particle in MeV for SM and NM as a function of the density and for the various interactions considered. The bands quantify the internal accuracy of the BHF calculation associated with the different 2BFs and 3BFs used.

dashed lines in the figure refer to fits of Skyrme interactions, which will be discussed in Sec. 4. In SM, the  $(0,0)$  channel is repulsive while the  $(1,0)$  and  $(0,1)$  channels are attractive. The  $(1,1)$  channel is much weaker than the others and could be attractive or repulsive depending on the 3BF interactions (it is slightly repulsive with 2BF and 2+3BFph). The 2+3BFmic approach has a density dependence strong enough to change the attractive  $(0,1)$  channel for 2BF into a repulsive one at high density, or to turn the repulsive  $(1,1)$  channel into an attractive one around  $n_{\text{sat}}$ . The  $(0,1)$  and  $(1,1)$  channels of NM are qualitatively similar to those of SM. The impact of the 3BF prescription can thus be opposite to the 2BF in the various channels. These features can be traced back to the general characteristics of the 3BF: the two-pion-exchange 3BF component is attractive in the  $(1,0)$  and repulsive in the  $(0,1)$  channel, and scalar repulsive 3BF components become dominant at high density in all channels.

It is also interesting to note that the 2+3BFmic approach has much wider error bars in the  $(S, T)$  decomposition of  $E_{\text{cor}}$  than in the total  $E_{\text{cor}}$  shown in Fig. 7 due to strong compensation between the different channels, which makes the total binding energy less dispersed than the  $(S, T)$  components.

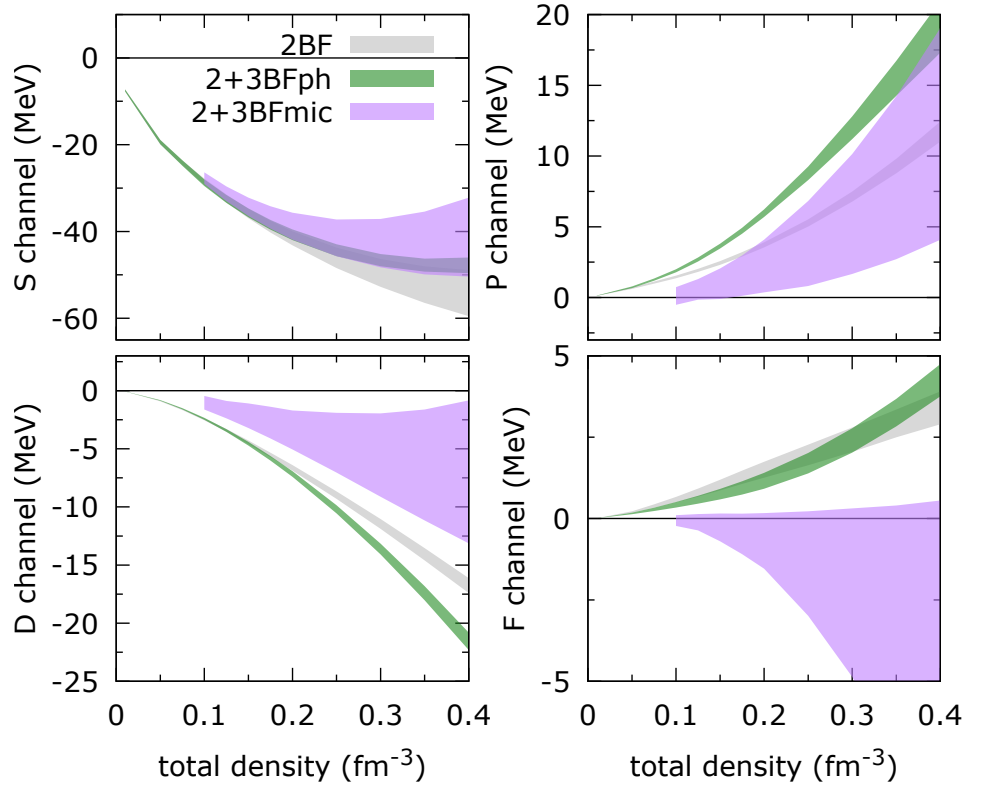


**Figure 2.** Decomposition in fixed- $L$  partial waves of the correlation energy per particle in SM as a function of the density for the various interactions.

### 3.1.2. Partial-wave decomposition of the correlation energy

Let us now further continue this analysis by looking in more detail at the partial-wave decomposition of  $E_{\text{cor}}$  for both SM and NM. The different partial waves contribute to the correlation energy as

$$E_{\text{cor}} = \sum_{LSJ} E_{\text{cor}}^{(LSJ)}, \quad (8)$$

where

$$E_{\text{cor}}^{(LSJ)} = \frac{(2J+1)}{4n(2\pi)^6} \sum_{\tau\tau'} \int d^3k_{\tau} f_{\tau}(\mathbf{k}_{\tau}) \int d^3k_{\tau'} f_{\tau'}(\mathbf{k}_{\tau'}) f_{\tau\tau'} \langle KqLSJ | G_{\tau\tau' \rightarrow \tau\tau'} | KqLSJ \rangle \quad (9)$$

with  $K = |\mathbf{k}_{\tau} + \mathbf{k}_{\tau'}|$ ,  $q = |(\mathbf{k}_{\tau} - \mathbf{k}_{\tau'})|/2$  and  $f_{\tau\tau'} = 1 + (-1)^{L+S} \delta_{\tau\tau'}$ .

We first show in Figs. 2 (for SM) and 3 (for NM) the decomposition into partial waves with fixed angular momentum  $L$ ,  $E_{\text{cor}}^{(L)} \equiv \sum_{SJ} E_{\text{cor}}^{(LSJ)}$ , i.e., all partial waves with the same value of  $L$  are summed together. Contributions up to a total angular momentum  $J = 8$  are considered in the calculation, although only results for the  $S, P, D$ , and  $F$  partial waves are shown, since the contributions of higher partial waves are small. It is indeed clear from the figures that the contributions of the different  $E_{\text{cor}}^{(L)}$  decrease as  $L$  increases for the range of densities considered here. Note that the  $P$  and  $D$  channels are found to be of the same order of magnitude in absolute value. Since the standard Skyrme EDF contributes only to the  $S$  and  $P$  channels, the relatively large importance of the  $D$  channel advocates for the extension of the standard Skyrme EDF as suggested in Ref. [28]. The  $F$  channel is found to be repulsive and less important than the others for 2BF and 2+3BFph, but strongly attractive and comparable to the  $D$  channel for 2+3BFmic. This corresponds to the  $(0,0)$  and  $(1,1)$  channels in Fig. 1.

The most significant difference between SM and NM is in the  $S$  channel, which is less attractive in NM compared to SM, due to the fact that the dominant attractive  ${}^3S_1$  channel

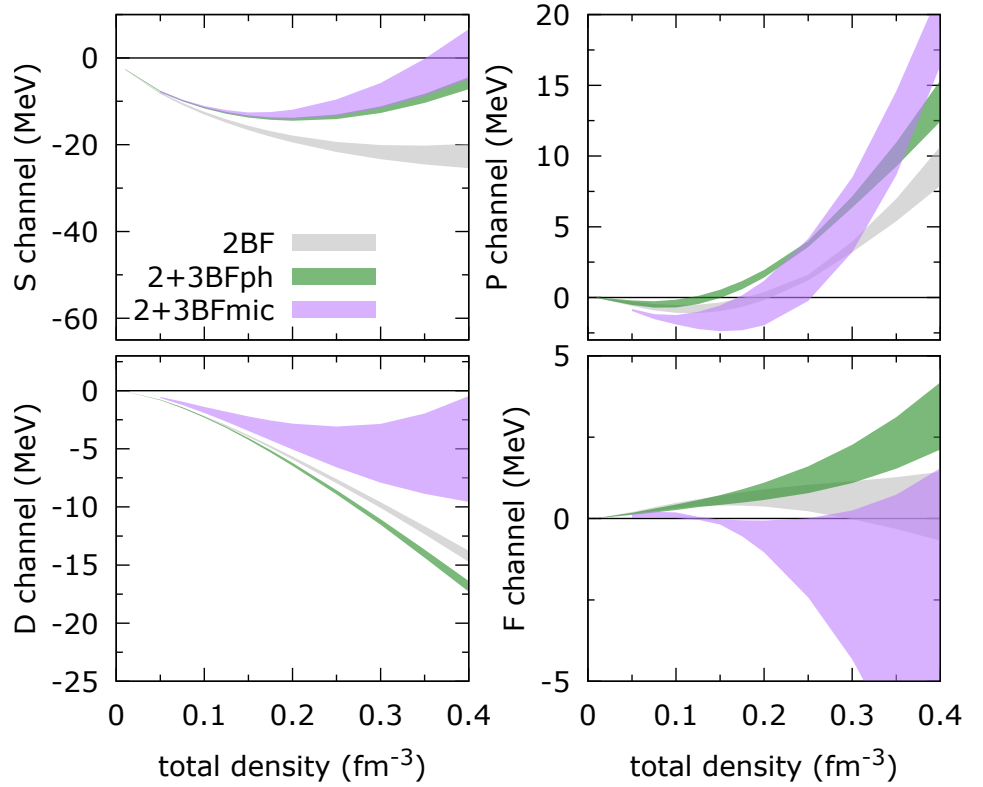


**Figure 3.** Same as Fig. 2 in NM.

contributes only to SM. The other channels are qualitatively similar in SM and NM. At low density  $n < n_{\text{sat}}$  one can clearly observe a dominance of the  $L = 0$  contribution compared to the  $L > 0$  terms, but as the density increases, those terms become increasingly important. As for the  $(S, T)$  decomposition, it is observed that the dispersion between the different predictions of the partial waves is generally larger in SM compared to NM.

Finally we present individual partial wave contributions to  $E_{\text{cor}}$  in Fig. 4, for the  $^1S_0$ ,  $^1P_1$ ,  $^3P_0$ ,  $^3P_1$ ,  $^3SD_1$  and  $^3PF_2$  waves. It is only in the  $^1S_0$  channel that the 3BF are similar, while in the other channels they act in opposite way compared to the 2BF results. The coupled  $^3SD_1$  and  $^3PF_2$  waves are predicted to be attractive in all cases, caused by the tensor force. Note that the standard Skyrme EDFs contribute only to the  $S$  and  $P$  channels, while in Ref. [28] the partial waves  $^3P_0$  and  $^3P_1$  have been used to calibrate the spin-orbit coupling  $W_0$  and the tensor parameter  $t_0^{(n)}$  of extended EDFs.

### 3.2. BHF single-particle energy

In the BHF approach, the s.p. energy  $\varepsilon_\tau(k)$  is defined by Eq. (2). In some phenomenological models however, like the Skyrme one, the momentum dependence of  $\varepsilon_\tau$  is simply quadratic and can be entirely incorporated in a modification of the mass appearing in the kinetic term,

$$\varepsilon_\tau(k) = \frac{k^2}{2m_\tau^*} + u_\tau, \quad (10)$$

where the effective mass  $m_\tau^*$  is a momentum-independent quantity and the s.p. potential  $u_\tau$  is the value of the s.p. potential at  $k = 0$ . Since we want to establish a link between microscopical and phenomenological approaches, using the BHF mean field potential  $U_\tau(k)$  one can define a global effective mass:

$$u_\tau = \text{Re}[U_\tau(k=0)], \quad (11)$$

$$\frac{m_\tau^*}{m} = \left[ 1 + \frac{2m}{k_{F_\tau}^2} \text{Re}[U_\tau(k_{F_\tau}) - U_\tau(0)] \right]^{-1}. \quad (12)$$



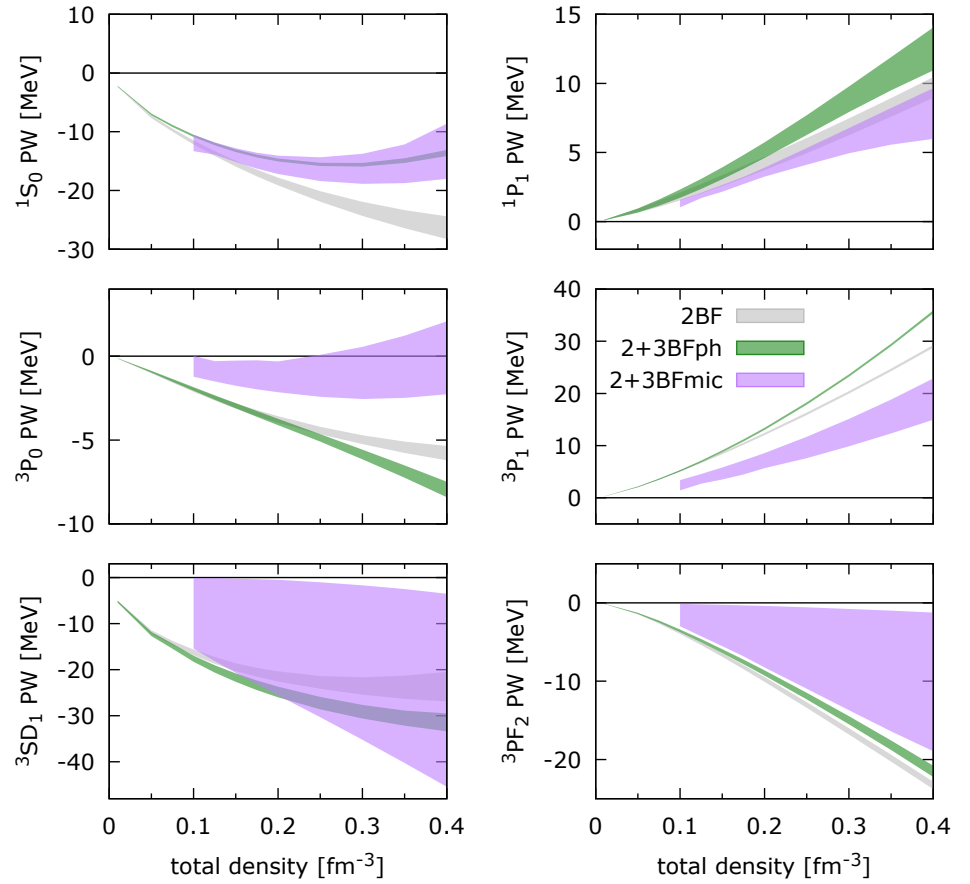


**Figure 4.** Contributions to the correlation energy per particle from various partial waves, as a function of the density for the different interactions.

Note that a local momentum-independent effective mass can also be determined from Eq. (4) as  $m_{\tau}^* = m_{\tau}^*(k = k_{F_{\tau}})$ . This latter definition provides effective masses which are typically 5-10% higher than using Eq. (12) at saturation density, due to the presence of a wiggle in the BHF s.p. potential close to  $k_F$  [49]. For the comparison with phenomenological models, we use the definition (12) for the global effective mass in the following.

The dependence of the effective mass on the isospin asymmetry is also an interesting result to extract from the BHF approach. One usually defines the effective-mass isospin splitting as

$$\Delta_{\beta}(n) \equiv \frac{m_n^*(n, \beta) - m_p^*(n, \beta)}{m}, \quad (13)$$

where  $n = n_n + n_p$  is the total density and  $\beta = (n_n - n_p)/n$  is the isospin asymmetry parameter.  $\Delta_{\beta}(n)$  is often defined for maximal asymmetry  $\beta = 1$  (NM) and at saturation density  $n = n_{\text{sat}}$ . Since this choice requires some technicalities for the definition of the proton effective mass in a pure neutron environment, we have preferred in this work to employ  $\Delta_{1/2}(n_{\text{sat}})$ , using the approximation  $\Delta_1 \approx 2\Delta_{1/2}$  [50]. Note that this relation is exact for Skyrme-type interactions, see Sec. 4.

The density dependence of the effective mass in symmetric matter  $m^*(n)/m$  and of the isospin splitting  $\Delta_{1/2}(n)$  are shown in Fig. 5, panels (a) and (b), respectively. At normal density the impact of 3BFs is small for both the effective mass and the isospin splitting. The effective mass is already well determined by 2BF only, that predict a continuous decrease of the effective mass and a positive sign for  $\Delta_{1/2}(n) \approx 0.03 \pm 0.03$  above  $n_{\text{sat}}$ . While the differences between 2+3BFph and 2+3BFmic predictions are small below saturation density, at larger density the 2+3BFmic results remain close to the 2BF ones, while 2+3BFph predict a rise of the effective mass and a change of sign of  $\Delta_{1/2}$  above  $2n_{\text{sat}}$ .

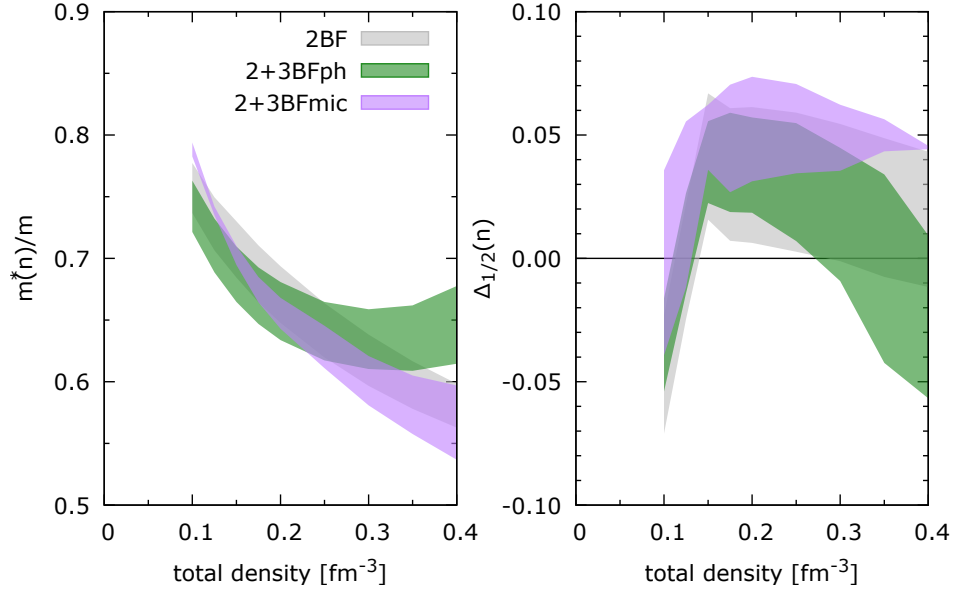


**Figure 5.** (left) Effective mass in SM and (right) isospin splitting of the effective mass for  $\beta = 0.5$  as a function of density for the various forces.

We therefore conclude that the momentum dependence of the 3BFph results is more marked than the one for 3BFmic. In the next subsection, we show that this is due to a compensation between two  $(S, T)$  contributions for 3BFmic, which is absent in the case of 3BFph. As a consequence, as the density increases 3BFph tends to reduce the correction due to the effective mass and the difference between the momentum-dependent contributions from neutrons and protons in asymmetric matter.

### 3.2.1. Spin-isospin decomposition of the effective mass

In Fig. 6 we show the spin-isospin decomposition of the inverse of the effective mass

$$\frac{m}{m_\tau^*} = 1 + \sum_{S,T} \left( \frac{m}{m_\tau^*} \right)^{(S,T)}, \quad (14)$$

where

$$\left( \frac{m}{m_\tau^*} \right)^{(S,T)} \equiv \frac{2m}{k_{F_\tau}^2} \text{Re} [U_\tau^{(S,T)}(k_{F_\tau}) - U_\tau^{(S,T)}(0)]. \quad (15)$$

being  $U_\tau^{(S,T)}(k)$  the contribution of the spin-isospin channel  $(S, T)$  to the s.p. mean field.

In the considered density range the inverse of the effective mass is dominated by the  $S$ -wave contributions in the  $(0, 1)$  and  $(1, 0)$  channels, where there is a reasonable agreement between the two 3BF prescriptions. Note that in the SM  $(0, 1)$  channel the two 3BF predict a increase of the inverse of the effective mass compared to the 2BF above  $n_{\text{sat}}$ : this originates from an attractive term in the 3BF, which moderates the repulsive contribution of the 2BF.

In the SM  $(1, 1)$  (and NM  $(S = 1)$ ) channels the 2+3BFmic has a stronger density dependence than 2+3BFph. The larger contribution to  $m/m^*$  indicates that there is an additional repulsive momentum dependence in 3BFmic that is absent from 3BFph. For 3BFmic, it happens that this additional repulsive contribution in the  $(1, 1)$  channel compensates the additional attraction in  $(0, 1)$ , such that the sum of all contributions to  $m/m^*$  is similar for 2BF and 2+3BFmic, as remarked in the discussion of Fig. 5. For 3BFph, the absence of the repulsive contribution in the  $(1, 1)$  channel induces the marked difference between 2BF and 2+3BFph for the inverse of the effective mass shown in Fig. 5. In the following, we show that the more repulsive 3BFmic leads also to more repulsion for the total energy per particle.

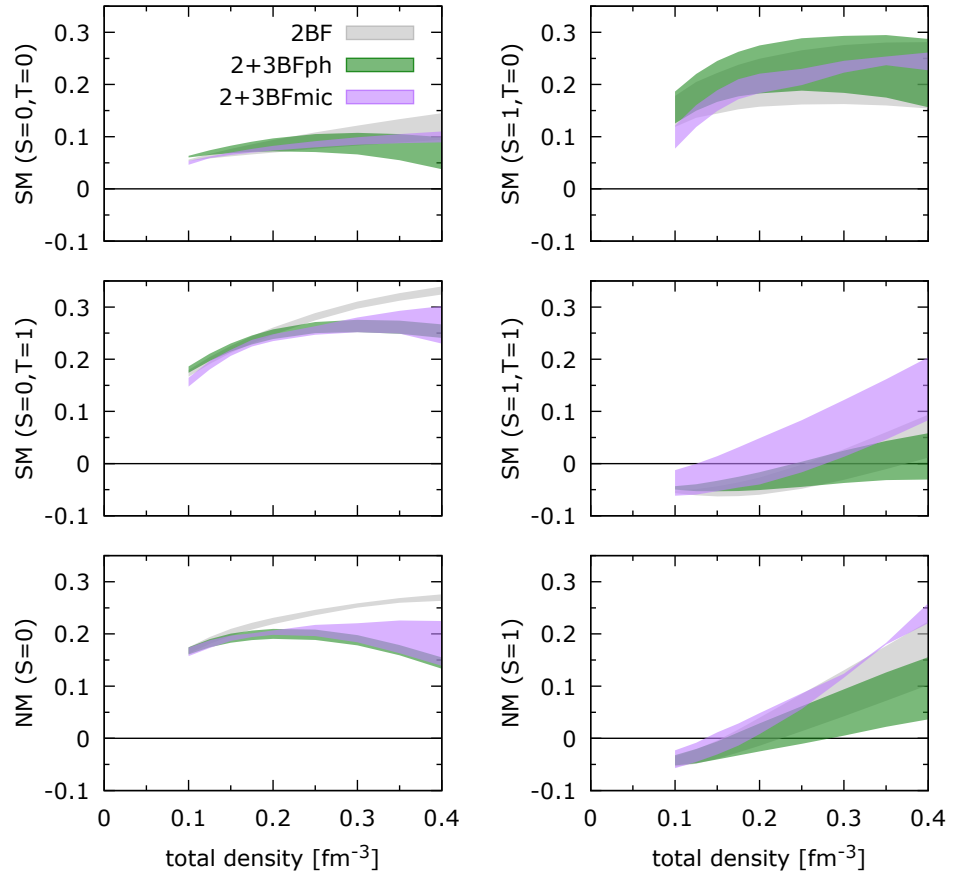


**Figure 6.** Spin-isospin decomposition of the effective mass  $(m/m^*)^{(S,T)}$ , Eq. (15), in SM and NM as a function of the density for various interactions.

### 3.3. Total energy

We show in Fig. 7 the correlation and total energy per particle of SM and NM as function of the density for the various 2BFs with and without the contribution of 3BFs. The SM results with only 2BF exhibit a saturation density well above the empirical value  $n_{\text{sat}}$ . This is well known and due to the different off-shell behavior of the 2BF: phase-shift-equivalent potentials lead to different saturation curves with the corresponding saturation points lying in the so-called “Coester band” [51]. The band defined by these curves can be used to estimate the contribution of 2BF to the uncertainty in the energy per particle. As expected the error bar is small at low densities, where the interaction is mainly dominated by the  $S$  partial waves, but increases rapidly with density, where higher partial waves become important. Similar behavior is observed for the 3BFph and 3BFmic results, and also for NM, where the uncertainty bands are narrower due to the weaker interaction. Above  $n_{\text{sat}}$  we observe that 2+3BFmic predict more repulsion than 2+3BFph, as discussed in the previous subsection.

At low density, our predictions are compared to  $\chi$ -EFT predictions based on 2+3BF calculated within different orders and approaches:

- (a) N2LO Wlazłowski QMC 2014 [52]: Variational QMC calculation of NM with chiral nuclear forces at N2LO for 2BF and 3BF.
- (b) N2LO Tews QMC 2016 [53]: AFDMC calculation of NM with chiral nuclear forces at N2LO for 2BF. The 3BF is taken at leading order and local.
- (c) N3LO Drischler MBPT 2016 [54]: Many-body perturbation theory approach based on regularized chiral nuclear forces at N3LO for SM and NM.

Note that while there are no uncertainties estimated in (a), the estimation of the uncertainty is performed differently in (b) and (c) compared to our BHF results. In those

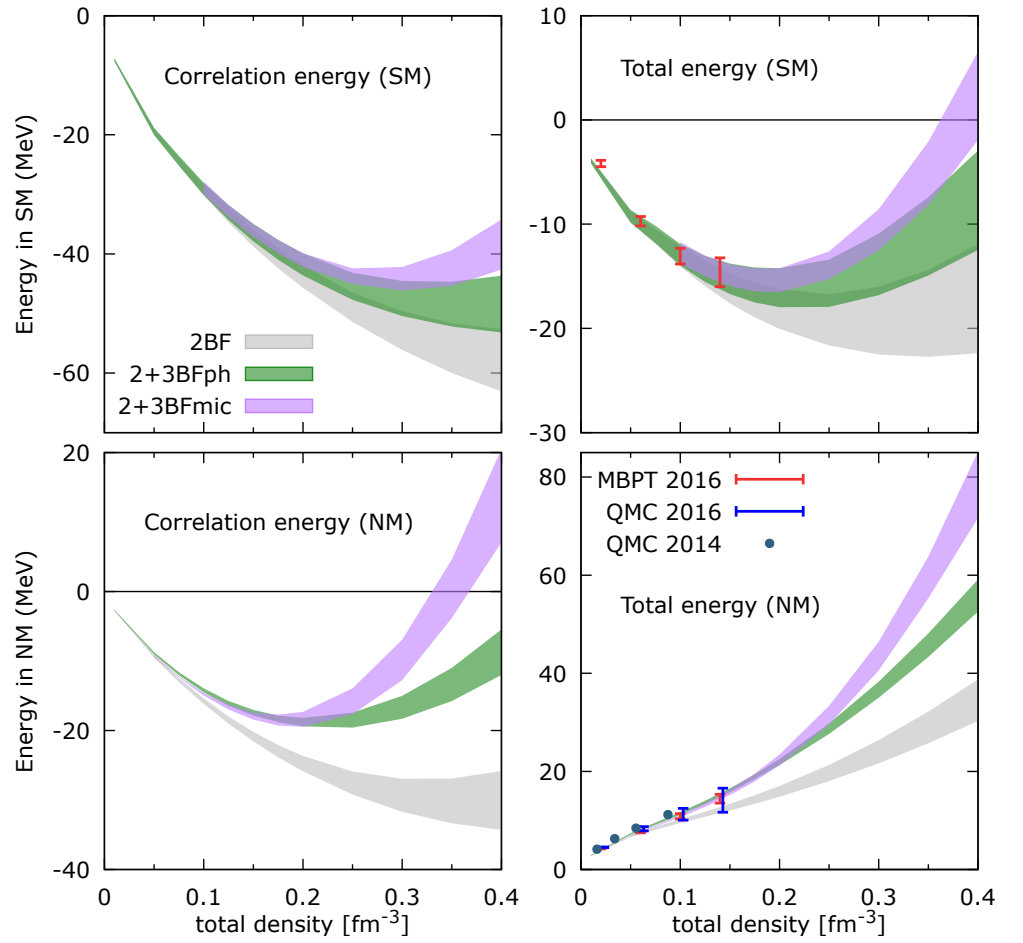


**Figure 7.** BHF correlation energy (left panels) and total energy (right panels) in SM (upper panels) and NM (lower panels) as a function of the density for the various  $NN$  potentials only (2BF) and including 3BF (2+3BFph, 2+3BFmic). Several  $\chi$ -EFT results [52–54] are also shown for comparison, see text for more details.

cases, the uncertainty includes the unknown from the chiral 2BF fitted on phase shifts as well as the uncertainty in the truncation order, which is expected to decrease as the order increases. Thus it is not surprising that the N3LO calculation [54] has slightly lower error bars than the N2LO one [53]. There are also differences in the way the band widths are estimated among these calculations. It is however interesting to note that the band of uncertainty in our case is compatible with the most advanced N3LO MBPT calculation [54] in both SM and NM. This provides a solid ground for our extrapolation to higher density, even if one cannot exclude an additional uncertainty related to the theoretical approach itself.

The conclusion of this part is that there are differences between the 3BF considered in this paper, 3BFph and 3BFmic, due to their different construction. The 3BFmic predict a more repulsive energy per particle than the 3BFph at high density.

#### 4. Constraining the Skyrme energy density functional from BHF calculations

The commonly called standard Skyrme interaction is a contact interaction with momentum-dependent terms, which is expressed in the following form,

$$\begin{aligned}
V(\mathbf{r}_1, \mathbf{r}_2) = & t_0(1 + x_0 P_\sigma) \delta(\mathbf{r}) \\
& + \frac{t_1}{2}(1 + x_1 P_\sigma) [\mathbf{k}'^2 \delta(\mathbf{r}) + \delta(\mathbf{r}) \mathbf{k}^2] \\
& + t_2(1 + x_2 P_\sigma) \mathbf{k}' \cdot \delta(\mathbf{r}) \mathbf{k} \\
& + \frac{t_3}{6}(1 + x_3 P_\sigma) n(\mathbf{R})^\gamma \delta(\mathbf{r}) \\
& + iW_0(\sigma_1 + \sigma_2) \cdot [\mathbf{k}' \times \delta(\mathbf{r}) \mathbf{k}], \tag{16}
\end{aligned}$$

where  $\mathbf{r} = \mathbf{r}_1 - \mathbf{r}_2$ ,  $\mathbf{R} = (\mathbf{r}_1 + \mathbf{r}_2)/2$ ,  $\mathbf{k} = (\nabla_1 - \nabla_2)/i$  is the relative momentum acting on the right,  $\mathbf{k}'$  its conjugate acting on the left, and  $P_\sigma = (1 + \sigma_1 \cdot \sigma_2)/2$  is the spin-exchange operator. The last term, proportional to  $W_0$ , corresponds to the zero-range spin-orbit term. It does not contribute to the EOS in homogeneous systems and thus will be ignored for the rest of this article. In its standard form (16) the Skyrme interaction contributes only in the  $L = 0$  and  $L = 1$  channels, which implies some limitations which will appear in the following discussion.

In the Hartree-Fock approximation, the total energy density of SM ( $\beta = 0$ ) and NM ( $\beta = 1$ ) is given respectively as

$$\varepsilon(n, \beta = 0) = \frac{1}{2m} \tau_{\text{SM}} + C_0^\tau n \tau_{\text{SM}} + C_0^n (n) n^2, \tag{17}$$

$$\varepsilon(n, \beta = 1) = \frac{1}{2m} \tau_{\text{NM}} + [C_0^\tau + C_1^\tau] n \tau_{\text{NM}} + [C_0^n(n) + C_1^n(n)] n^2, \tag{18}$$

where the kinetic densities are  $\tau_{\text{SM}} = \frac{3}{5}(\frac{3\pi^2}{2})^{2/3} n^{5/3}$  and  $\tau_{\text{NM}} = \frac{3}{5}(3\pi^2)^{2/3} n^{5/3}$ , and  $C_t^n(n) = C_{t0}^n + C_{t3}^n n^\gamma$  for  $t = 0, 1$ . In this work, we employ the DFT coefficients, e.g.  $C_t^\tau$ ,  $C_{t0}^n$ , and  $C_{t3}^n$ , which can be defined in terms of the Skyrme parameters  $t_i$  and  $x_i$ , see Ref. [55], where they have been introduced.

Several authors (see, e.g., Refs. [10,25–27]) have stressed the interest of using the spin-isospin decomposition of the BHF correlation energy as an additional constraint to better determine the parameters of energy density functionals based on effective interactions such as the Skyrme one. It indeed allows a more detailed determination of the parameters entering into the calculation of the energy per particle by increasing the number of equations to solve. From Eq. (7), one can calculate the decomposition of the correlation energy density in terms of SE  $\varepsilon_{\text{cor}}^{(0,1)}$ , TE  $\varepsilon_{\text{cor}}^{(1,0)}$ , SO  $\varepsilon_{\text{cor}}^{(0,0)}$ , and TO  $\varepsilon_{\text{cor}}^{(1,1)}$  contributions as [26]

$$\begin{aligned}
\varepsilon_{\text{cor}}^{(0,0)} &= \frac{1}{16} [C_0^\tau - 3C_0^{sT} - 3C_1^\tau + 9C_1^{sT}] n \tau_{\text{SM}}, \\
\varepsilon_{\text{cor}}^{(0,1)} &= \frac{3}{4} [C_0^n(n) + C_1^n(n)] n^2 + \frac{3}{16} [C_0^\tau - 3C_0^{sT} + C_1^\tau - 3C_1^{sT}] n \tau_{\text{SM}}, \\
\varepsilon_{\text{cor}}^{(1,0)} &= \frac{1}{4} [C_0^n(n) - 3C_1^n(n)] n^2 + \frac{3}{16} [C_0^\tau + C_0^{sT} - 3C_1^\tau - 3C_1^{sT}] n \tau_{\text{SM}}, \\
\varepsilon_{\text{cor}}^{(1,1)} &= \frac{9}{16} [C_0^\tau + C_0^{sT} + C_1^\tau + C_1^{sT}] n \tau_{\text{SM}} \tag{19}
\end{aligned}$$

in SM, and as

$$\begin{aligned}
\varepsilon_{\text{cor}}^{(0)} &= [C_0^n(n) + C_1^n(n)] n^2 + \frac{1}{4} [C_0^\tau - 3C_0^{sT} + C_1^\tau - 3C_1^{sT}] n \tau_{\text{NM}} \\
\varepsilon_{\text{cor}}^{(1)} &= \frac{3}{4} [C_0^\tau + C_0^{sT} + C_1^\tau + C_1^{sT}] n \tau_{\text{NM}} \tag{20}
\end{aligned}$$

in NM. The correlation energy in the channels (0,0) and (1,1) in SM, and (1) in NM scales only with the kinetic energy,  $\tau_{SM}$  and  $\tau_{NM}$ , because only the angular momentum  $L = 1$  can contribute in these channels. In the channels (0,1) and (1,0) in SM, and (0) in NM, there is also a term that scales with the density  $n$  reflecting the  $L = 0$  contribution of the Skyrme interaction. Depending on the sign of the combination of the coefficients, the energy per particle in the  $(S, T)$  channels can be positive or negative, in the channels (0,0) and (1,1) in SM, and (1) in NM, or can change its sign as a function of the density in the other channels. This is a clear limitation of the standard Skyrme interaction (16), since BHF calculations predict a richer density dependence, see Fig. 1 for instance.

In nuclear matter, the Skyrme interaction is determined by 8 coefficients  $C_t^\tau$ ,  $C_t^{sT}$ ,  $C_{t0}^\rho$ , and  $C_{t3}^\rho$ , as well as the exponent of the density dependence  $\gamma$ . We have 6 constraints in terms of the  $(S, T)$  decomposition and we decide to fix the value of the parameter  $\gamma$ , see hereafter. We therefore need two additional constraints to determine unambiguously all Skyrme parameters. These two other constraints will be given by the effective mass in SM and the isospin splitting, namely from the BHF predictions we fix  $m_{sat}^*/m = 0.7$  and  $\Delta_{1,sat} = 0.1$  for 2BF, 2+3BFph, and 2+3BFmic.

For the Skyrme interaction, the nucleon effective mass is expressed as [26,55]

$$\frac{1}{2m_\tau^*(n, \beta)} = \frac{1}{2m} + [C_0^\tau + \tau_3 C_1^\tau \beta] n. \quad (21)$$

The parameters  $C_0^\tau$  and  $C_1^\tau$  can therefore be obtained as

$$C_0^\tau = \frac{1}{n_{sat}} \frac{1}{2m} \left[ \frac{m}{m_{sat}^*} - 1 \right], \quad (22)$$

$$C_1^\tau = \frac{1}{n_{sat}} \frac{1}{2m} \frac{1}{\beta \Delta_\beta} \left[ 1 - \sqrt{1 + \left( \frac{\Delta_\beta}{m_{sat}^*/m} \right)^2} \right] \quad (23)$$

$$\approx -\frac{1}{n_{sat}} \frac{1}{2m} \frac{\Delta_\beta}{2\beta} \left( \frac{m}{m_{sat}^*} \right)^2, \quad (24)$$

where the last approximation is valid for typical small values of  $\left( \frac{\Delta_\beta}{m_{sat}^*/m} \right)^2 \approx 0.02$ .

We determine the 8 Skyrme coefficients by imposing the global reproduction of the 6  $(S, T)$  channels predicted by the BHF calculations in the density range going from 0.01 up to 0.4 fm<sup>-3</sup> in SM and NM (including uncertainties), complemented by the effective mass  $m_{sat}^*/m$  and its isospin splitting  $\Delta_{1,sat}$ . The fit is provided by the nonlinear least-squares Marquardt-Levenberg algorithm encoded in Gnuplot<sup>2</sup>. The results are shown in Fig. 8, where the parameter  $\gamma$  is explored from 1 to 1/10. The error bars are estimated from the covariant matrix properties at the solution. There are 4 Skyrme coefficients  $C_t^\tau$  and  $C_t^{sT}$ , with  $t = 0, 1$ , which are independent of  $\gamma$ , and 4 other coefficients  $C_{t0}^\rho$  and  $C_{t3}^\rho$ , which depend on the value taken for  $\gamma$ . We also observe a strong impact of the 3BF for the coefficient  $C_1^{sT}$ , and a noticeable but less strong impact for the coefficients  $C_{t0}^\rho$  and  $C_{t3}^\rho$ .

In order to evaluate the quality of the fits, we compare in Fig. 9 the quantities targeted by our fits and the results provided by our fits. The Skyrme spin-isospin  $(S, T)$  channel decomposition of the correlation energy per particle in SM and NM are shown together with the constraints extracted from BHF calculations. We consider the centroid of the Skyrme coefficients obtained from Fig. 8 and vary the parameter  $\gamma$ . The effect of  $\gamma$  is very weak since it is absorbed in the values of the coefficients  $C_{t0}^\rho$  and  $C_{t3}^\rho$ , see Fig. 8. The other four coefficients  $C_t^\tau$  and  $C_t^{sT}$  are independent of  $\gamma$ . The quality of the fit is however not very good. This is particularly clear in the following channels: (0,0), (1,1) in SM and (1) in NM. These channels are the ones where only the  $L = 1$  contribution of the Skyrme interaction plays a role. The poor reproduction of the BHF results is therefore due to the

<sup>2</sup> see [https://gnuplot.sourceforge.net/docs\\_4.2/node82.html](https://gnuplot.sourceforge.net/docs_4.2/node82.html)

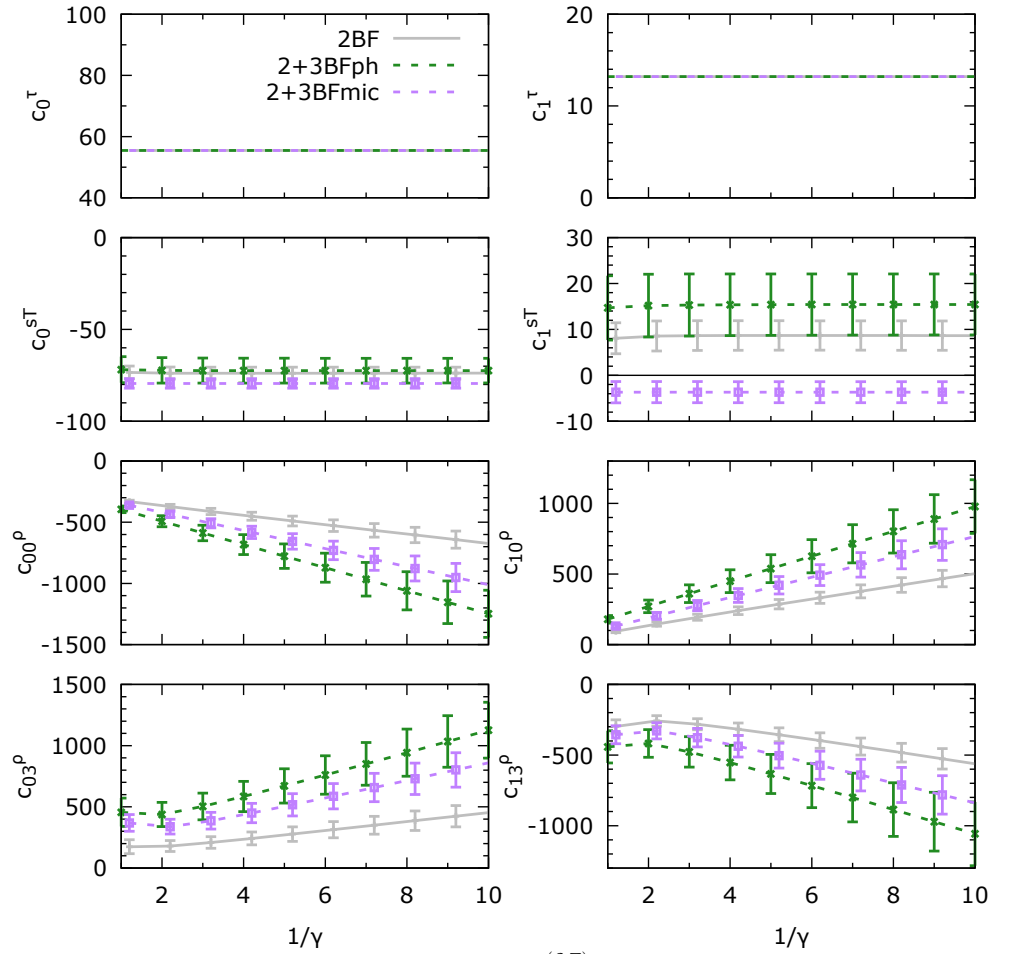


**Figure 8.** Skyrme coefficients obtained from the fit of  $\varepsilon_{\text{cor}}^{(S,T)}$  and the effective mass as function of  $1/\gamma$ . The models are calibrated to the following quantities;  $m_{\text{sat}}^*/m = 0.7$  and  $\Delta_{1,\text{sat}} = 0.1$ , and to the BHF correlation energies in the  $(S, T)$  channels in SM and  $(S)$  channels in NM.

lack of flexibility of the standard form (16) of the Skyrme interaction, where higher values of  $L$  are necessary.

Let us remark from Fig. 9 that the 2BF is quite well reproduced by the Skyrme model in SM and for the  $(0, 0)$ ,  $(0, 1)$  and  $(1, 0)$  channels. The  $(1, 1)$  channel has a wrong sign in the Skyrme model, although the strength of the interaction in this channel is quite weak. In NM, however, the fit of the 2BF is poor above  $n_{\text{sat}}$ . We, therefore, conclude that already at the 2BF level the Skyrme interaction could not reproduce well the BHF predictions in both SM and NM above  $n_{\text{sat}}$ .

In Ref. [10], a set of Skyrme interactions have been obtained by employing the  $(S, T)$  decomposition in SM for two BHF calculations and the NM channel was controlled globally by variational calculations. The difference with our approach are i) that our uncertainty estimate is based on a larger number of calculations, and ii) that we employ the  $(S)$  channel decomposition in NM to adjust Skyrme EDF. In Ref. [27], only one BHF calculation is employed to fit the Skyrme EDF and only the  $(S, T)$  decomposition in SM is employed. In Refs. [10,27] data from finite nuclei, e.g. binding energies and charge radii, have been employed in addition to the BHF constraints. It is therefore difficult to perform detailed comparisons of our results with the ones presented in these papers. We however conclude from our analysis that the standard Skyrme EDF should be enriched, with higher  $L$  terms for instance, in order to reproduce BHF calculations in  $(S, T)$  channel in SM and NM up to at least  $0.4 \text{ fm}^{-3}$ . The results presented in this paper can be employed for such aim.

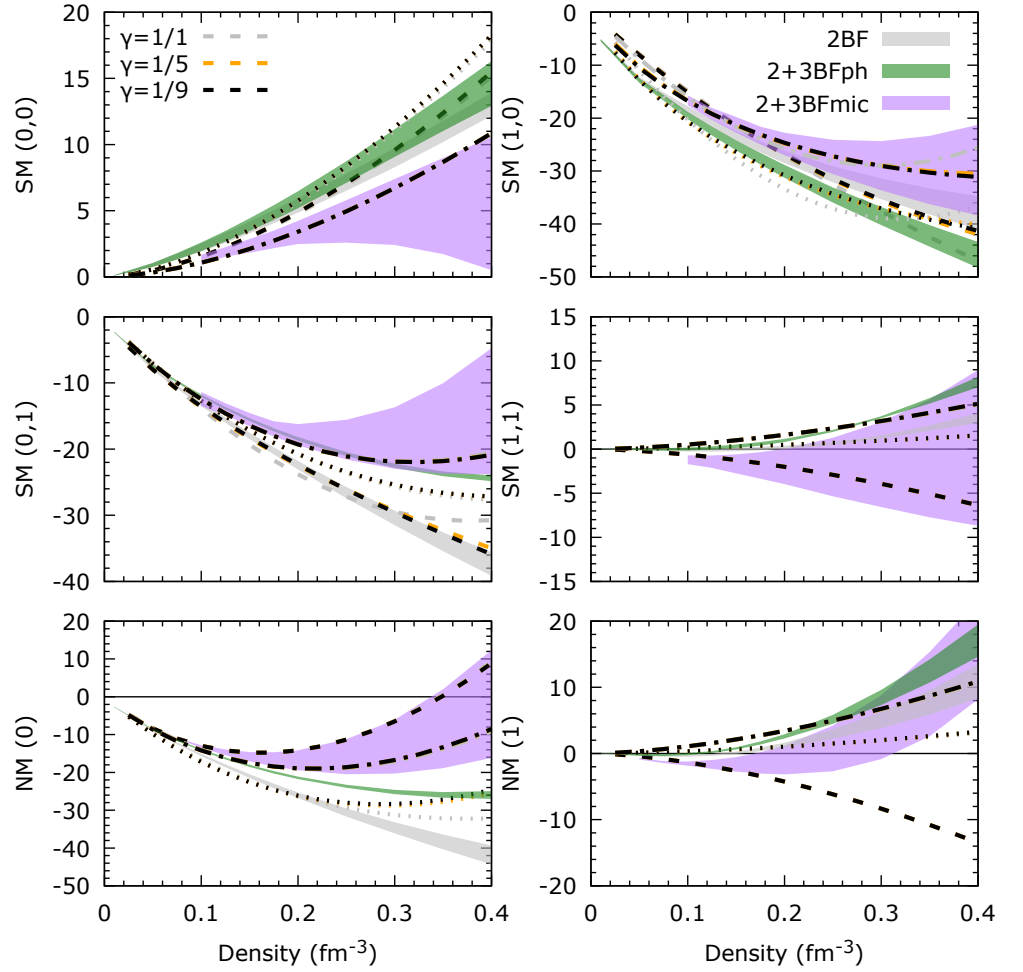


**Figure 9.** Spin-isospin ( $S, T$ ) channel decomposition of the correlation energy per particle in SM and NM as a function of the density for the various interactions considered. The bands quantify the internal accuracy of the BHF calculation associated with the different 2BFs and 3BFs used. The curves are the result of the fit of the Skyrme EDF: the dashed lines represent fits of 2BF, dotted of 2+3BFph, and dashed-dotted of 2+3BFmic.

## 5. Conclusions

In this paper, we have analyzed BHF results of SM and NM by decomposing the total energy and the effective mass into spin-isospin ( $S, T$ ) channels and also into contributions from various partial waves. The two-body and three-body contributions were shown separately as bands representing the uncertainties after exploring a set of interactions. We found that 3BFmic induces more repulsion than 3BFph, visible in the energy per particle at high density. This repulsion originates from a stronger repulsive scalar-meson-exchange term of 3BFmic compared to 3BFph. The effective mass, however, seems to be more impacted by 3BFph than by 3BFmic. We show that this results from a compensation between two channels in 3BFmic which is absent for 3BFph.

We have then addressed the question of the effectiveness of the standard Skyrme model (16) to reproduce the ( $S, T$ ) decompositions predicted by BHF calculations based on different 2BFs and 3BFs. Our results indicate that the standard Skyrme model can not reproduce the ( $S, T$ ) decomposition predicted by BHF calculations above  $n_{\text{sat}}$  considering only 2BF. This conclusion is even stronger when 3BFs are added.

The detailed and numerous quantities obtained from BHF calculations and presented in this paper can however serve as guidelines for improvements of the Skyrme interaction with close links to BHF calculations. Having reliable models to describe the properties of



baryonic matter at extreme densities on the one hand, and fair estimates of the theoretical uncertainties on the other hand, are important for the treatment of the astrophysical signals that will be collected in the future.

**Author Contributions:** All authors contributed to this work. All authors have read and agreed to the published version of the manuscript.

**Funding:** JM is partially supported by CNRS-IN2P3 MAC masterproject, as well as from the LABEX Lyon Institute of Origins (ANR-10-LABX-0066).

**Acknowledgments:** This work was also fostered by the scientific emulation created by the “New-CompStar” COST Action MP1304 and PHAROS COST Action MP16214.

**Conflicts of Interest:** The authors declare no conflicts of interest.

## References

1. B. Abbott et al., *Phys. Rev. Lett.* **119**, 161101 (2017).
2. B. P. Abbott et al., *Astrophys. J. Lett.* **848**, L13 (2017).
3. S. Weinberg, *Physica A* **96**, 327 (1979); S. Weinberg, *Phys. Lett.* **B251**, 288 (1990); S. Weinberg, *Nucl. Phys. B* **363**, 3 (1991); E. Epelbaum, H.-W. Hammer, and U.-G. Meißner, *Rev. Mod. Phys.* **81**, 1773 (2009); R. Machleidt and D. R. Entem, *Phys. Rep.* **503**, 1 (2011).
4. J. Margueron, R. Hoffmann Casali, and F. Gulminelli, *Phys. Rev.* **C97**, 025805 (2018).
5. K. Hebeler, J. M. Lattimer, C. J. Pethick, and A. Schwenk, *Astrophys. J.* **773**, 11 (2013).
6. I. Tews, J. Carlson, S. Gandolfi, and S. Reddy, *Astrophys. J.* **860**, 149 (2018).
7. C. Drischler, K. Hebeler, and A. Schwenk, *Phys. Rev. Lett.* **123**, 042501 (2019).
8. S. K. Bogner, T. T. S. Kuo, and L. Coraggio, *Nucl. Phys. A* **684**, 432c (2001); S. K. Bogner, T. T. S. Kuo, and A. Schwenk, *Phys. Rep.* **386**, 1 (2003).
9. E. Chabanat, P. Bonche, P. Haensel, J. Meyer, and R. Schaeffer, *Nucl. Phys. A* **627**, 710 (1997); *ibid.* **635**, 231 (1998).
10. S. Goriely, N. Chamel, and J. M. Pearson, *Phys. Rev. C* **82**, 035804 (2010); *ibid.* **88**, 024308 (2013).
11. A. Fantina, N. Chamel, J. M. Pearson, S. Goriely, *Astron. & Astrophys.* **559**, A128 (2013).
12. M. Baldo, A. Polls, A. Rios, H.-J. Schulze, and I. Vidaña, *Phys. Rev.* **C86**, 064001 (2012).
13. M. Baldo, *Nuclear Methods and the Nuclear Equation of State*, International Review of Nuclear Physics, Vol. 8 (World Scientific, Singapore, 1999); H.-J. Schulze, J. Cugnon, A. Lejeune, M. Baldo, and U. Lombardo, *Phys. Rev. C* **52**, 2785 (1995).
14. H. Q. Song, M. Baldo, G. Giansiracusa, and U. Lombardo, *Phys. Rev. Lett.* **81**, 1584 (1998); M. Baldo, G. Giansiracusa, U. Lombardo, and H. Q. Song, *Phys. Lett.* **B473**, 1 (2000); M. Baldo, A. Fiasconaro, H. Q. Song, G. Giansiracusa, and U. Lombardo, *Phys. Rev.* **C65**, 017303 (2001); R. Sartor, *Phys. Rev.* **C73**, 034307 (2006); M. Baldo and C. Maieron, *J. Phys.* **G34**, R243 (2007); M. Baldo and C. Maieron, *Phys. Rev.* **C72**, 034005 (2005); K. Fukukawa, M. Baldo, G. F. Burgio, L. Lo Monaco, and H.-J. Schulze, *Phys. Rev.* **C92**, 065802 (2015).
15. W. H. Dickhoff and C. Barbieri, *Prog. Part. Nucl. Phys.* **52**, 377 (2004); T. Frick, H. Müther, A. Rios, A. Polls, and A. Ramos, *Phys. Rev. C* **71**, 014313 (2005); V. Somà and P. Božek, *Phys. Rev. C* **74**, 045809 (2006); **78**, 054003 (2008); A. Rios, A. Polls, and I. Vidaña, *Phys. Rev. C* **79**, 025802 (2009).
16. S. Gandolfi, A. Y. Illarionov, K. E. Schmidt, F. Pederiva, and S. Fantoni, *Phys. Rev. C* **79**, 054005 (2009); S. Gandolfi, F. Pederiva, S. Fantoni, and K. E. Schmidt, *Phys. Rev. Lett.* **98**, 102503 (2007).
17. J. Carlson, J. Morales, V. R. Pandharipande, and D. G. Ravenhall, *Phys. Rev. C* **68**, 025802 (2003).
18. V. R. Pandharipande and R. B. Wiringa, *Rev. Mod. Phys.* **51**, 821 (1979); S. Fantoni and A. Fabrocini, in *Microscopic Quantum Many-Body Theories and Their Applications*, edited by J. Navarro and A. Polls (Springer-Verlag, Berlin, 1998), Lecture Notes in Physics, Vol. 510; A. Lovato, O. Benhar, S. Fantoni, A. Y. Illarionov, and K. E. Schmidt, *Phys. Rev. C* **83**, 054003 (2011); R. B. Wiringa, V. Fiks, and A. Fabrocini, *Phys. Rev. C* **38**, 1010 (1988).
19. R. B. Wiringa and S. C. Pieper, *Phys. Rev. Lett.* **89**, 182501 (2002).
20. R. B. Wiringa, V. G. J. Stoks, and R. Schiavilla, *Phys. Rev.* **C51**, 38 (1995).
21. M. Piarulli, I. Bombaci, D. Logoteta, A. Lovato, and R. B. Wiringa, *Phys. Rev. C* **101**, 045801 (2020).
22. A. Lovato, I. Bombaci, D. Logoteta, M. Piarulli, and R. B. Wiringa, *Phys. Rev. C* **105**, 055808 (2022).
23. M. Baldo, C. Maieron, P. Schuck, and X. Viñas, *Nucl. Phys. A* **736**, 241 (2004).

24. M. Baldo, P. Schuck, and X. Viñas, *Phys. Lett. B* **663**, 390 (2008); M. Baldo, L. Robledo, P. Schuck, and X. Viñas, *J. Phys. G: Nucl. Phys.* **37**, 064015 (2010); M. Baldo, L. Robledo, P. Schuck, and X. Viñas, *Phys. Rev. C* **87**, 064305 (2013).
25. L. G. Cao, U. Lombardo, C. W. Shen, and N. Van Giai, *Phys. Rev. C* **73**, 014313 (2006).
26. T. Lesinski, K. Bennaceur, T. Duguet, and J. Meyer, *Phys. Rev. C* **74**, 044315 (2006).
27. D. Gambacurta, L. Li, G. Colò, U. Lombardo, N. Van Giai, and W. Zuo, *Phys. Rev. C* **84**, 024301 (2011).
28. D. Davesne, J. Navarro, P. Becker, R. Jodon, J. Meyer, and A. Pastore, *Phys. Rev. C* **91**, 064303 (2015).
29. W. Khon and L. J. Sham, *Phys. Rev. Lett.* **140**, 1133 (1965).
30. X. R. Zhou, G. F. Burgio, U. Lombardo, H.-J. Schulze, and W. Zuo, *Phys. Rev.* **C69**, 018801 (2004);
31. Z. H. Li and H.-J. Schulze, *Phys. Rev.* **C78**, 028801 (2008).
32. A. Roggero, A. Mukherjee, and F. Pederiva, *Phys. Rev. C* **92**, 054303 (2015).
33. B. D. Day, *Rev. Mod. Phys.* **39**, 719 (1967); M. Baldo, in *Nuclear Methods and the Nuclear Equation of State*, M. Baldo (Ed.), World Scientific, Singapore, 1999.
34. J. P. Jekeunne, A. Lejeunne, and C. Mahaux, *Phys. Rep.* **25**, 83 (1976).
35. J. J. Lu, Z. H. Li, C. Y. Chen, M. Baldo, and H.-J. Schulze, *Phys. Rev.* **C96**, 044309 (2017).
36. Z. H. Li and H.-J. Schulze, *Phys. Rev.* **C94**, 024322 (2016).
37. R. B. Wiringa, V. G. J. Stoks, and R. Schiavilla, *Phys. Rev. C* **51**, 38 (1995).
38. Th. A. Rijken, V. G. J. Stoks, and Y. Yamamoto, *Phys. Rev. C* **59**, 21 (1999); V. G. J. Stoks and Th. A. Rijken, *Phys. Rev. C* **59**, 3009 (1999).
39. R. Machleidt, K. Holinde, and Ch. Elster, *Phys. Rep.* **149**, 1 (1987); R. Machleidt, *Ad. Nucl. Phys.* **19**, 189 (1989).
40. R. Machleidt, F. Sammarruca, and Y. Song, *Phys. Rev. C* **53**, 1483 (R) (1996).
41. B. S. Pudliner, V. R. Pandharipande, J. Carlson, and R. B. Schiavilla, *Phys. Lett. B* **74**, 4396 (1995).
42. J. Fujita and H. Miyazawa, *Prog. Theor. Phys.* **17**, 360 (1957).
43. X. R. Zhou, G. F. Burgio, U. Lombardo, H.-J. Schulze, and W. Zuo, *Phys. Rev.* **C69**, 018801 (2004);
44. V. G. J. Stoks, R. A. M. Klomp, C. P. F. Terheggen, and J. J. de Swart, *Phys. Rev. C* **49**, 2950 (1994).
45. B. A. Loiseau, Y. Nogami, and C. K. Ross, *Nucl. Phys. A* **165**, 601 (1971); *Nucl. Phys. A* **176**, 665 (E) (1971); P. Grangé, M. Martzloff, Y. Nogami, D. W. L. Sprung, and C. K. Ross, *Phys. Lett. B* **60**, 237 (1976); M. Baldo and L. Ferreira, *Phys. Rev. C* **59**, 682 (1999).
46. Z. H. Li, U. Lombardo, H.-J. Schulze, and W. Zuo, *Phys. Rev.* **C77**, 034316 (2008);
47. Z. H. Li and H.-J. Schulze, *Phys. Rev.* **C78**, 028801 (2008).
48. D. Logoteta, I. Vidaña, I. Bombaci, and A. Kievsky, *Phys. Rev.* **C91**, 064001 (2015);
49. X. L. Shang, A. Li, Z. Q. Miao, G. F. Burgio, and H.-J. Schulze, *Phys. Rev.* **C101**, 065801 (2020).
50. W. Zuo, L. G. Cao, B. A. Li, U. Lombardo, and C. W. Shen, *Phys. Rev. C* **72**, 014005 (2005).
51. Z. H. Li, U. Lombardo, H.-J. Schulze, W. Zuo, L. W. Chen, and H. R. Ma, *Phys. Rev.* **C74**, 047304 (2006).
52. G. Wlazłowski, J.W. Holt, S. Moroz, A. Bulgac, K.J. Roche, *Phys. Rev. Lett.* **113**, 182503 (2014).
53. I. Tews, S. Gandolfi, A. Gezerlis, A. Schwenk, *Phys. Rev.* **C93**, 024305 (2016).
54. C. Drischler, K. Hebeler, A. Schwenk, *Phys. Rev.* **C93**, 054314 (2016).
55. M. Bender, P.-H. Heenen, and P.-G. Reinhard, *Rev. Mod. Phys.* **75**, 121 (2003); J. R. Stone and P.-G. Reinhard, *Prog. Part. Nucl. Phys.* **58**, 587 (2007); J. Erler, P. Klüpfel, and P.-G. Reinhard, *J. Phys.* **G38**, 033101 (2011).